

Assessing the Importance of Noise from Thermal Sunyaev-Zel'dovich Signals for CMB Cluster Surveys and Cluster Cosmology

SRINIVASAN RAGHUNATHAN¹

¹*Center for Astrophysical Surveys, National Center for Supercomputing Applications, Urbana, IL 61801, USA*

ABSTRACT

We explore the significance of noise from thermal Sunyaev-Zel'dovich (tSZ) signals for cluster detection using cosmic microwave background (CMB) surveys. The noise arises both from neighboring objects and also from haloes below the detection limit. A wide range of surveys are considered: SPT-SZ, SPTpol, and SPT-3G from the South Pole Telescope; SO-Baseline and SO-Goal configurations for Simons Observatory; CMB-S4's wide area (S4-Wide) and deep (S4-Ultra deep) surveys; and the futuristic CMB-HD experiment. We find that the noise from tSZ signals has a significant impact on CMB-HD and to some extent on S4-Ultra deep. For other experiments, the effect is negligible as the noise in the tSZ map is dominated by residual foregrounds or experimental noise. In the limit when the noise from tSZ signals is important, we find that removing the detected clusters and rerunning the cluster finder allows us to find a new set of less massive and distant clusters. Since the detected clusters are the dominant source of the tSZ power, removing them reduces the power at $\ell = 3000$ by: $\times 5$ for CMB-HD; $\times 3.1$ of S4-Ultra deep; $\times 2.4$ for S4-Wide and SPT-3G; $\times 1.5$ for SO-Goal and SPTpol; $\times 1.35$ for SO-Baseline; and $\times 1.08$ for SPT-SZ. We forecast the expected number of clusters and also derive parameter constraints by combining cluster counts with primary CMB and tSZ power spectra finding that the future surveys can reduce the error on the dark energy equation of state parameter to sub-percent levels and can also enable $\geq 3\sigma$ detection of the sum of neutrino masses. The simulation products and results can be downloaded from this [link](#)[🔗].

1. INTRODUCTION

The thermal Sunyaev-Zel'dovich (tSZ) effect (Sunyaev & Zel'dovich 1970) is a result of the inverse Compton scattering of cosmic microwave background (CMB) photons off free electrons in the hot intracluster medium (ICM). The signal has emerged as a strong probe of both the structure formation as well as the complex ICM gas-trophysics. For example, see works by Komatsu & Seljak (2002); Shaw et al. (2009); Battaglia et al. (2012); Reichardt et al. (2012); Hill & Pajer (2013); Horowitz & Seljak (2017); Bolliet et al. (2018); Douspis et al. (2021) for astrophysical and cosmological constraints using the angular power spectrum of the tSZ and Holder et al. (2007); Bhattacharya et al. (2012); Hill & Sherwin (2013); Crawford et al. (2014); Hurier & Lacasa (2017) for statistics other than tSZ power spectrum. Besides these, the tSZ effect is also one of the most efficient methods used for detecting galaxy clusters (see catalogs from Bleem et al. 2015; Planck Collaboration et al.

2016a; Hilton et al. 2020; Huang et al. 2020; Bleem et al. 2020). The abundance of clusters as a function of mass and redshift can also place tight constraints on the parameters that govern structure formation and geometry of the Universe (Holder et al. 2001; Lima & Hu 2004; Allen et al. 2011; Sartoris et al. 2012; Mak & Pierpaoli 2013) like, for example, dark energy equation of state w_0 , normalization of the matter power spectrum σ_8 , and the sum of neutrino masses $\sum m_\nu$ as demonstrated using data (recently by Zubeldia & Challinor 2019; Bocquet et al. 2019; Planck Collaboration et al. 2020; To et al. 2021; Costanzi et al. 2021; Mantz et al. 2021; Salvati et al. 2021). Thanks to its redshift independent nature (Sunyaev & Zel'dovich 1970), the tSZ effect allows us to detect clusters at high redshifts where the signal-to-noise (S/N) of other cluster observables like richness estimates or X-ray flux drop rapidly. As a result, the tSZ-selected cluster samples from CMB surveys are highly complementary to large catalogs of $z \lesssim 1.5$ clusters expected from the future optical, infrared, and X-ray surveys (LSST Science Collaboration et al. 2009; Laureijs et al. 2011; Merloni et al. 2012).

With the improvement in noise levels of the current (Benson et al. 2014; Henderson et al. 2016; Bender et al. 2018) and future (The Simons Observatory Collaboration et al. 2018; CMB-S4 Collaboration 2019; Sehgal et al. 2019) CMB experiments, the sample size of the tSZ-selected clusters is expected to increase several fold compared to the existing catalogs (Louis & Alonso 2017; Madhavacheril et al. 2017; Gupta et al. 2020; Raghunathan et al. 2021). However, as we are approaching these unprecedented map depths, the effect of astrophysical foreground signals also become important. Although the frequency dependent nature of the foreground signals can help us mitigate them using multi-frequency information, one of the irreducible components is the noise from tSZ signals of other haloes, both along the line-of-sight (LOS) and also the confusion noise from the ones below the detection limit of the experiment. We collectively refer to both these sources as the tSZ-noise in the rest of the paper. Holder et al. (2007) explored the impact of the tSZ-noise and found it to be important for future surveys when the mass thresholds approach $M_{vir} \sim 1.2 \times 10^{14} h^{-1} M_{\odot}$. The authors, however, did not include the effects of other sources of variance like the astrophysical foregrounds, CMB, and the experimental noise in their study.

In this work, we reassess the importance of the tSZ-noise for a wide range of CMB (past, current, and future) experiments namely: SPT-SZ, SPTpol, and SPT-3G surveys from the South Pole Telescope (SPT) and the upcoming experiments namely Simons Observatory (SO), CMB-S4, and CMB-HD. For SO, we consider two configurations: SO-Baseline and SO-Goal (The Simons Observatory Collaboration et al. 2018). For CMB-S4, we use both the wide-area survey (S4-Wide) from Chile and the smaller but deeper delensing survey (S4-Ultra deep) from the South Pole (CMB-S4 Collaboration 2019). Our simulations include the effect of experimental noise and the astrophysical foregrounds. We find that the tSZ-noise has no impact on cluster surveys from SPT-SZ, SPTpol, SO-Baseline and SO-Goal; and a negligible impact on SPT-3G and S4-Wide. The effect of tSZ confusion noise is mildly important for S4-Ultra deep but significantly affects CMB-HD. For all surveys, we also show the impact of masking the detected clusters in the tSZ power spectrum. When the tSZ-noise affects cluster finding, we find that removing the detected clusters and rerunning the cluster detection algorithm allows us to detect less massive and distant clusters lying near the same LOS. Finally, we compute the expected number of clusters and the cosmological constraints by combining cluster abundance measurements with primary CMB and tSZ power spectra.

The paper is structured as follows. In §2, we describe our simulations: CMB and astrophysical foregrounds in §2.1, noise in §2.2, tSZ signals in §2.3 and §2.4. The cluster detection method is given in §3. We present the formalism to get cluster counts and Fisher forecasts in §4, results in §5, and conclude in §6. Finally, we provide details about the cluster S/N calculation in Appendix A.

The cluster masses in this work are reported with respect to the radius R_{500c} which encompasses the region within which the average mass density is 500 times the critical density of the Universe at the cluster redshift z . We adopt the flat-sky approximation and replace spherical harmonic transforms by Fourier transforms since we are dealing with small regions of the sky. The relation between the Fourier wavenumber k and the multipole ℓ is given by $k = \sqrt{k_x^2 + k_y^2} = \ell/2\pi$. The underlying cosmology used was set to *Planck* 2015 measurements (TT + lowP in Table 4 of Planck Collaboration et al. 2016b).

2. SIMULATIONS

In this section, we briefly describe the simulations and cluster detection method used in this work and point the reader to Raghunathan et al. (2021, referred to as R21 hereafter) for more details. The simulation setup is similar to R21 other than the tSZ simulations and noise models for experiments not considered in that work.

2.1. CMB and astrophysical foregrounds

We generate $120' \times 120'$ wide realizations of the millimetre wave temperature sky with a pixel resolution of $0.5'$. The simulated components include: CMB; instrumental and atmospheric noise; astrophysical foregrounds namely emission from radio point sources, dusty star-forming galaxies (DSFG) which we refer to as the cosmic infrared background (CIB), diffuse kinematic SZ (kSZ) and tSZ signals, and the tSZ signal from the cluster under study. For simplicity, we ignore signals from galactic foregrounds but note that they can affect large-scale Compton- y measurements and hence have non-negligible impact only on massive low redshift cluster detections (R21). The simulated maps are convolved with a band-dependent Gaussian instrumental beam. The instrumental specifications and the number of frequency bands for the experiments are given in Table 1. We note that the pixel resolution adopted here is sub-optimal for the CMB-HD experiment and hence our results must be treated as conservative estimates. We perform Gaussian simulations of an underlying power spectrum for CIB, CMB, kSZ, noise and radio galaxies. For tSZ, we use a different approach as described in §2.3.

To simulate the CMB, we use **CAMB** (Lewis et al. 2000) software to obtain the LSS lensed power spectra C_ℓ^{TT} for the fiducial *Planck* 2015 cosmology. Modeling of the atmospheric and instrumental noise spectra is described in §2.2. For astrophysical foregrounds namely CIB, kSZ, and radio galaxies, we use power spectra measured at 150 GHz by the SPT experiment (George et al. 2015) and simply scale them to other bands. Note that the power from CIB, kSZ, and radio galaxies are dominated by the diffuse signals below the detection limit and as a result performing Gaussian realizations is a reasonable thing to do. To scale the spectrum of the radio galaxies for sources with flux $S_{150} < 6.4$ mJy which is the SPT masking threshold (George et al. 2015; Reichardt et al. 2021), we use a power law with spectral index $\alpha_{\text{radio}} = -0.6$ (Everett et al. 2020). For CIB, we use the

spectral energy distribution (SED) scaling parameterized using a modified blackbody as $\eta_\nu = \nu^{\beta_{\text{CIB}}} B_\nu(T_{\text{CIB}})$ where $T_d = 20$ K is the temperature and $B_\nu(T)$ is the *Planck* function. We use two different emissivity indices $\beta_{\text{CIB-PO}} = 1.505$ and $\beta_{\text{CIB-CI}} = 2.51$ for the Poisson and the clustered components of the CIB signal respectively (George et al. 2015). The masking threshold used for DSFG is the same as radio galaxies ($S_{150} = 6.4$ mJy) for all experiments except CMB-HD. For CMB-HD, we follow Sehgal et al. (2019) and reduce the level of CIB by $\times 17$ at 150 GHz. This is to account for the template based subtraction of sources with flux above $S_{150} \geq 0.04$ mJy using higher S/N detections of the same sources at 270/350 GHz bands (Sehgal et al. 2019). Since the kSZ has the same blackbody spectrum as the CMB, we do not apply any frequency scaling for the diffuse kSZ signals.

Table 1. Instrumental specifications for different experiments considered in this study.

Experiment	f_{sky}	Beam θ_{FWHM} [arcminutes]							Δ_T [$\mu\text{K-arcmin}$]						
		30	40	90	150	220	270	350	30	40	90	150	220	270	350
SPT-SZ	6%	-	-	1.7	1.2	1.0	-	-	-	-	41.0	18.0	80.0	-	-
SPTpol	1.2%	-	-	1.7	1.2	-	-	-	-	-	12.0	5.5	-	-	-
SPT-3G	3.6%	-	-	1.7	1.2	1.0	-	-	-	-	3.0	2.2	8.8	-	-
SO-Baseline	40%	7.4	5.1	2.2	1.4	1.0	0.9	-	71.0	36.0	8.0	10.0	22.0	54.0	-
SO-Goal	40%	7.4	5.1	2.2	1.4	1.0	0.9	-	52.0	27.0	5.8	6.3	15.0	37.0	-
S4-Wide	67%	7.3	5.5	2.3	1.5	1.0	0.8	-	21.8	12.4	2.0	2.0	6.9	16.7	-
S4-Ultra deep	3%	8.4	5.8	2.5	1.6	1.1	1.0	-	4.6	2.94	0.45	0.41	1.29	3.07	-
CMB-HD	50%	1.4	1.05	0.45	0.25	0.20	0.15	0.12	6.5	3.4	0.73	0.79	2.0	2.7	100

2.2. Noise models

Experimental noise can be decomposed into two: atmospheric and instrumental noise components. The combined noise power spectrum is modeled as

$$N_\ell = N_{\ell,\text{white}} + N_{\ell,\text{atm}} \left(\frac{\ell}{\ell_{\text{knee}}} \right)^{-\alpha_{\text{knee}}}. \quad (1)$$

The first term $N_{\ell,\text{white}}$ represents the instrumental noise as given in Table 1 for different experiments (Bleem et al. 2015; Henning et al. 2018; Bender et al. 2018; The Simons Observatory Collaboration et al. 2018; CMB-S4

Collaboration 2019; Sehgal et al. 2019). The rest of the terms, $N_{\ell,\text{atm}}$, ℓ_{knee} , and α_{knee} are used to model the atmospheric noise. For CMB-HD, CMB-S4 and SPT (SPT-3G, SPTpol, and SPT-SZ) experiments we set $N_{\ell,\text{atm}} = N_{\ell,\text{white}}$ and the values used for ℓ_{knee} and α_{knee} are provided in Table 2. For SO, we adopt the same prescription given in The Simons Observatory Collaboration et al. (2018) by using $N_{\ell,\text{red}}$ and setting $\ell_{\text{knee}} = 1000$ and $\alpha_{\text{knee}} = 3.5$ (Louis et al. 2017). The values for $N_{\ell,\text{red}}$ in $\mu\text{K}^2\text{s Sr}^{-1}$ for SO large aperture telescopes (LAT) are picked from Table 2 of The Simons Observatory Collaboration et al. (2018). We convert $N_{\ell,\text{red}}$ in $\mu\text{K}^2\text{s Sr}^{-1}$ to $N_{\ell,\text{atm}}$ in μK^2 units using the procedure detailed in §2.2 of The Simons Observatory Collabora-

Table 2. Atmospheric $1/f$ noise specifications (ℓ_{knee} , α_{knee}) for SPT (SPT-3G, SPTpol, and SPT-3G), CMB-S4, and CMB-HD experiments. For SPTpol, we do not include the 220 GHz band in line with Table 1.

Band [GHz]	SPT ^a	S4-Ultra deep ^b	S4-Wide ^c	CMB-HD ^c
30	-	1200, 4.2	471, 3.5	
40		1200, 4.2	478, 3.5	
90	1200, 3.0	1200, 4.2	2154, 3.5	
150	2200, 4.0	1900, 4.1	4364, 3.5	
220	2300, 4.0	2100, 3.9	7334, 3.5	
270	-	2100, 3.9	7308, 3.5	
350		-	-	7500, 3.5

^aCheck Appendix of Aylor et al. (2019).

^bCheck V3R025 configuration in https://cmb-s4.uchicago.edu/wiki/index.php/Delensing_sensitivity_-_updated_sensitivities,_beams,_TT_noise.

^chttps://cmb-s4.uchicago.edu/wiki/index.php/Expected_Survey_Performance_for_Science_Forecasting.

tion et al. (2018) as

$$N_{\ell,\text{atm}} = N_{\ell,\text{red}} \frac{A_{\text{sky}}}{t_{\text{obs}}}. \quad (2)$$

Here the sky area is $A_{\text{sky}} = 4\pi f_{\text{sky}}$ [Sr] and $f_{\text{sky}} = 0.4$ as given in Table 1. The total observation time is $t_{\text{obs}} = N_{\text{total}} \eta_{\text{obs-eff}} \eta_{\text{map-cuts}}$ where $N_{\text{total}} = 5$ years is the survey period expressed in seconds, $\eta_{\text{obs-eff}} = 0.2$ is the observing efficiency, and $\eta_{\text{map-cuts}} = 0.85$ represents the data cuts to account to $\sim 15\%$ noisy map edges (The Simons Observatory Collaboration et al. 2018).

2.3. Thermal SZ simulations

The main goal of this work is to understand the importance of the noise from the tSZ signals of haloes other than the cluster under consideration. Like mentioned earlier, the tSZ-noise can arise both from adjacent haloes near the LOS and also from the haloes below the detection limit of the experiment. While it is reasonable to perform Gaussian realizations of the diffuse tSZ signals below the detection threshold, assuming the same for all haloes can degrade the cluster detection sensitivity. This is because the number counts of clusters follow a random Poisson distribution on the sky, which is highly non-Gaussian, and the total map variance is dominated by a few pixels with clusters. Here and throughout, when we refer to non-Gaussian nature of the tSZ signals, we simply refer to the non-Gaussian tails in the Poisson distribution and not to any other higher point correlations, which are assumed to be absent in this

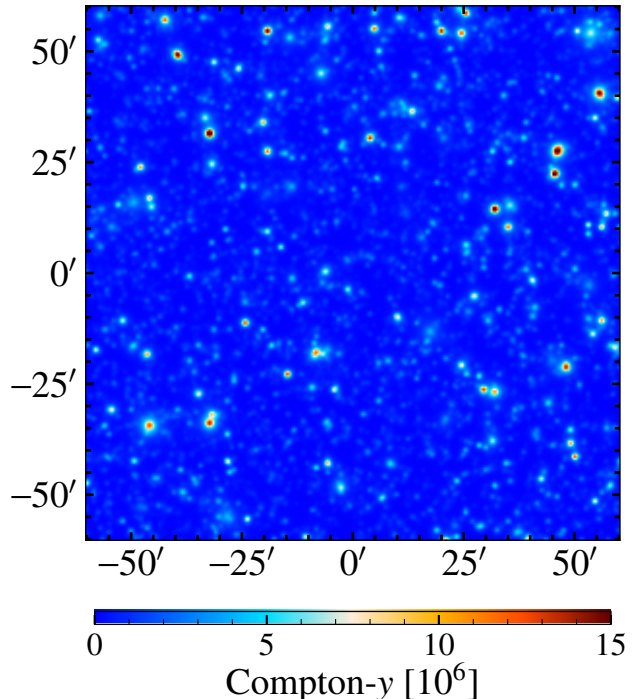


Figure 1. An example of the $120' \times 120'$ Poisson tSZ simulation produced in this work. The simulation contains signal from all clusters with $M_{500c} \geq 10^{13} M_{\odot}$ in the redshift range $z \in [0.1, 4.0]$. The tSZ signal of a given halo is modeled using the generalized NFW profile as described in §2.4 and the signal arising due to clustering of clusters has been ignored.

study. Subsequently, we generate Poisson realizations of the $120' \times 120'$ tSZ sky by considering all haloes with $M_{500c} \geq 10^{13} M_{\odot}$ in the redshift range $z \in [0.1, 4.0]$.

To this end, we adopt the Tinker et al. (2008) halo mass function (HMF) to first generate a map of the number counts and paste cluster tSZ signal of the corresponding halo $y(M_{500c}, z)$ as described below in §2.4. The simulations do not include contributions from clustering of clusters, the *2-halo term*, since it has been found to be negligible in the angular scales (see Fig. 1 of Komatsu & Kitayama 1999) and mass range (see Fig. 1 and Fig. 7 of Hill et al. 2018) considered in this work. However, we also note that this is strictly true only for tSZ power spectrum measurements since the presence of clustering can increase the local variance and might have an impact on the cluster detection. We leave a careful investigation of this to a future study. Fig. 1 shows an example of the Poisson-tSZ simulation generated in this study. The average Compton- y power spectrum from 500 Poisson realizations is shown as the black solid curve in Fig. 2. While our simulations predict a higher power compared to the values reported by ACT, *Planck*, and SPT, the power spectrum is in

good agreement with the publicly available BAHAMAS¹ simulations (McCarthy et al. 2017, 2018) shown as the orange solid curve. We show the measured values by ACT (Dunkley et al. 2013) as blue triangle, *Planck* (Tanimura et al. 2022) as yellow diamonds, SPT-SZ (George et al. 2015) as green square, and the combination of SPT-SZ and SPTpol (Reichardt et al. 2021) as red circle. The fiducial BAHAMAS model shown here includes astrophysical feedback which pushes the gas out from the haloes reducing the power on small-scales compared to the case without feedback effects (Shaw et al. 2010; McCarthy et al. 2014). Since our simulations do not include such astrophysical effects, the black curve is higher than the orange BAHAMAS model on small-scales. Note that we do not perform any normalization using BAHAMAS and the match between black and orange curves around $\ell \sim 3000$ is just a coincidence. On large-scales, the power spectrum is slightly lower than *Planck* and BAHAMAS primarily because of the minimum cluster redshift $z = 0.1$ adopted in this work but also due to absence of the clustering term. We ignore such large-scale effects since those scales are less important for clusters expected from future CMB surveys.

Once the tSZ simulations are produced, we inject the tSZ signals using three different approaches in our simulated maps. In the first case, we simply add the generated Poisson realizations (see Fig. 1 for an example) and this is referred as Poisson-tSZ case throughout this work. In the second (Gaussian-tSZ) case, we use the fiducial power spectrum shown as black solid curve in Fig. 2 and produce Gaussian realizations of them. The difference in the results between the above two cases shows the importance of the non-Gaussian nature of the tSZ. We also compare the results from Poisson-tSZ case to the results from simulations where the tSZ signals are completely ignored (no-tSZ). This quantifies the impact of the tSZ-noise on cluster detection.

2.4. Cluster tSZ signal

The cluster tSZ signal is modeled using a generalized Navarro-Frenk-White (NFW, Navarro et al. 1996; Zhao 1996) as proposed by Nagai et al. (2007) and calibrated using X-ray observations by Arnaud et al. (2010). The dimensionless pressure profile $P_e(l, x)$ of the ICM is integrated along the LOS to obtain the Compton- y signal $y(x)$ which is then converted into CMB temperature

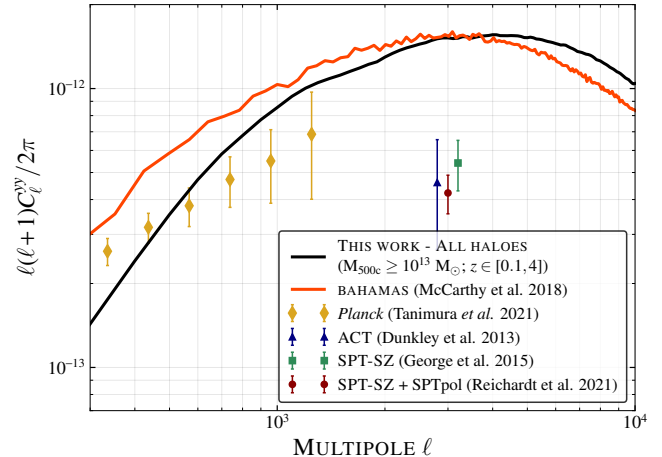


Figure 2. The black solid curve is the average Compton- y power spectrum, expressed as D_ℓ^{yy} , from 500 Poisson simulations generated in this work. The orange curve is the power spectrum computed using the publicly available BAHAMAS simulations for the fiducial model (McCarthy et al. 2018). For reference, we also show the measurements from *Planck* as yellow diamonds (Planck Collaboration et al. 2016c), ACT as blue triangle (Dunkley et al. 2013), SPT-SZ and SPTpol as green square (George et al. 2015) and red circle (Reichardt et al. 2021).

units as

$$P_e(l, x) = \frac{P_0}{(c_{500}x)^\gamma [1 + (c_{500}x)^\alpha]^{(\frac{\beta-\gamma}{\alpha})}} \quad (3)$$

$$y(x) = \frac{\sigma_T}{m_e c^2} \int_l P_e(l, x) dl$$

$$\delta_T = y(x) g_{SZ}(\nu) T_{\text{CMB}} K.$$

The frequency dependence of the tSZ signal (Itoh et al. 1998; Chluba et al. 2012) is

$$g_{SZ}(\nu) = x \coth(x/2) - 4 \text{ with } x = \frac{h\nu}{k_B T_{\text{CMB}}}. \quad (4)$$

In the above equations, $c_{500}x = r/r_s$ where c_{500} is the concentration parameter, r_s is the scale radius, and $x = r/R_{500}$ is the distance to cluster center expressed in terms of R_{500} ; c in the velocity of light, m_e is the mass of the electron, σ_T in the Thomson cross section, $T_{\text{CMB}} = 2.73$ K is the mean temperature of the CMB; h and k_B are the Planck and Boltzmann constants respectively. Using the generalization of the Planck Collaboration et al. (2016c) $Y_{SZ} - M$ relation by Louis & Alonso (2017); Madhavacheril et al. (2017) to include mass and redshift evolution, we obtain the integrated cluster Compton Y_{SZ500c} by integrating $y(x)$ over the angular extent of the cluster R_{500} as

¹ We pick the fiducial BAHAMAS model for the *Planck* 2015 cosmology from <https://www.astro.ljmu.ac.uk/~igm/BAHAMAS/>

$$Y_{\text{SZ}_{500c}} = Y_* \left[\frac{H_0}{70} \right]^{-2+\alpha_Y} \left[\frac{(1-b_{\text{HSE}})M_{500c}}{M_*} \right]^{\alpha_Y} \quad (5)$$

$$e^{\beta_Y \log^2(\frac{M_{500c}}{M_*})} \left[\frac{D_A(z)}{100\text{Mpc}} \right]^2 E^{2/3}(z) (1+z)^{\gamma_Y},$$

along with a log-normal scatter

$$\sigma_{\log Y}(M_{500c}, z) = \sigma_{\log Y,0} \left[\frac{M_{500c}}{M_*} \right]^{\alpha_\sigma} (1+z)^{\gamma_\sigma}. \quad (6)$$

We adopt the same pivotal mass $M_* = 6 \times 10^{14} M_\odot$ as Planck Collaboration et al. (2016c) and subsequently set the normalization factor $\log Y_* = -0.19$ and the mass evolution parameter $\alpha_Y = 1.79$. The hydrostatic equilibrium (HSE) mass bias parameter is assumed to be constant across all redshifts and set to $b_{\text{HSE}} = 0.2$ (Zubeldia & Challinor 2019; Makiya et al. 2020). The angular diameter distance to the cluster at redshift z and the Hubble function are represented using $D_A(z)$ and $E(z) = H(z)/H_0$ respectively. The fiducial value for the scatter is set to $\sigma_{\log Y,0} = 0.127$ (Louis & Alonso 2017; Madhavacheril et al. 2017). The second order mass evolution β_Y and redshift evolution γ_Y parameters of the $Y_{\text{SZ}} - M$ relation in Eq.(5) and the mass α_σ and redshift γ_σ evolution parameters of the scatter Eq.(6) are all fixed to be zero.

3. CLUSTER DETECTION

Similar to R21, we perform an optimal internal linear combination (ILC) of maps M from different frequency channels N_{ch} to construct a minimum variance (MV) Compton- y map that is fed into a maximum likelihood estimator (MLE) for S/N calculation. In Fourier space, the ILC operation corresponds to $y_\ell = \sum_{i=1}^{N_{\text{ch}}} w_\ell^i M_\ell^i$. We obtain the optimal multipole dependent weights w_ℓ for each frequency channel using the SMICA (Spectral Matching Independent Component Analysis) algorithm (Cardoso et al. 2008; Remazeilles et al. 2011; Planck Collaboration et al. 2014) as

$$w_\ell = \frac{\mathbf{C}_\ell^{-1} \mathbf{a}}{\mathbf{a}^T \mathbf{C}_\ell^{-1} \mathbf{a}}, \quad (7)$$

where \mathbf{C}_ℓ is the covariance between the simulated maps in multiple frequencies at a given multipole ℓ with dimension $N_{\text{ch}} \times N_{\text{ch}}$, $\mathbf{a} = [-5.33, -5.23, -4.36, -2.61, 0.09, 2.27, 5.95]$ is the frequency response vector of the Compton- y signal for [30, 40, 90, 150, 220, 270, 350] GHz channels shown in Eq.(4).

In Fig. 3 we show the weights w_ℓ for all channels used to construct the MV Compton- y map from different ex-

periments. Since we are mainly interested in the tSZ-noise, we do not use constrained ILC algorithms (Remazeilles et al. 2011) as done in Madhavacheril et al. (2020); Bleem et al. (2021). For details about the effect of CIB / radio galaxy contamination on the recovered tSZ signals, we refer the reader to look into R21. We can note from the figure that 90 and 150 GHz channels mostly dominate the weights as expected. The weights for higher frequency channels ($\nu \geq 220$ GHz) are significantly smaller since they are mainly used to reduce the variance from the CIB signals. The lower frequency bands, 30/40 GHz, have a much larger beam than 90/150 GHz channels and only contribute on large-angular scales to reduce the variance from atmospheric noise.

The sum of the weighted noise and foregrounds signals, $N_\ell^{yy} = \frac{1}{\mathbf{a}^T \mathbf{C}_\ell^{-1} \mathbf{a}}$, referred generally as residual noise in the Compton- y maps are presented in Fig. 4. The grey band in the figure represents the 1σ and 2σ errors from (George et al. 2015) and the fiducial value in the figure is set to mean value from 500 Poisson simulations performed in this work (same as black solid curve in Fig. 2). On small scales, the residuals are much lower for CMB-HD compared to other experiments because of the reduced level of CIB signals (see §2.1) expected in the CMB-HD maps (Sehgal et al. 2019). The other experiments are limited by foregrounds signals, primarily CIB, or instrumental noise. On large-scales, in the absence of galactic foregrounds as is the case here, atmospheric noise and CMB dominate the residuals. They can be lowered further by including information from the *Planck* satellite. From the figure, we can see that SPT-3G and S4-Wide will be sample variance limited near the peak $3000 \leq \ell \leq 5000$ of the Compton- y spectrum and map those scales with $S/N \geq 1$. The residual noise in the Compton- y maps for S4-Ultra deep and CMB-HD are much lower than the other experiments and the fiducial signal level. As a result, we can suppose the tSZ-noise to have a significant impact on the cluster survey from CMB-HD and to some extent from S4-Ultra deep compared to other experiments as we show in §5.1.

We feed the MV Compton- y map into the MLE to estimate the S/N of clusters as a function of M_{500c} and redshift z . We calculate

$$-2 \ln \mathcal{L} = \sum_{ij} (\hat{\mathbf{y}}_i - \mathbf{y}_i^{\text{th}}) \hat{\mathbf{C}}_{ij}^{-1} (\hat{\mathbf{y}}_j - \mathbf{y}_j^{\text{th}}), \quad (8)$$

where $\mathbf{y}_i \equiv \mathbf{y}_i(\theta)$ is the azimuthally-averaged profile of the Compton- y signal in bins i of $\Delta\theta = 0.5$. The models \mathbf{y}^{th} used for fitting the measured Compton- y signal $\hat{\mathbf{y}}$, are calculated using Eq.(5). We set $\theta_{\text{max}} = 2'$ since $\theta_{\text{max}} \geq R_{500c}/D_A(z)$ encompasses the tSZ signal from

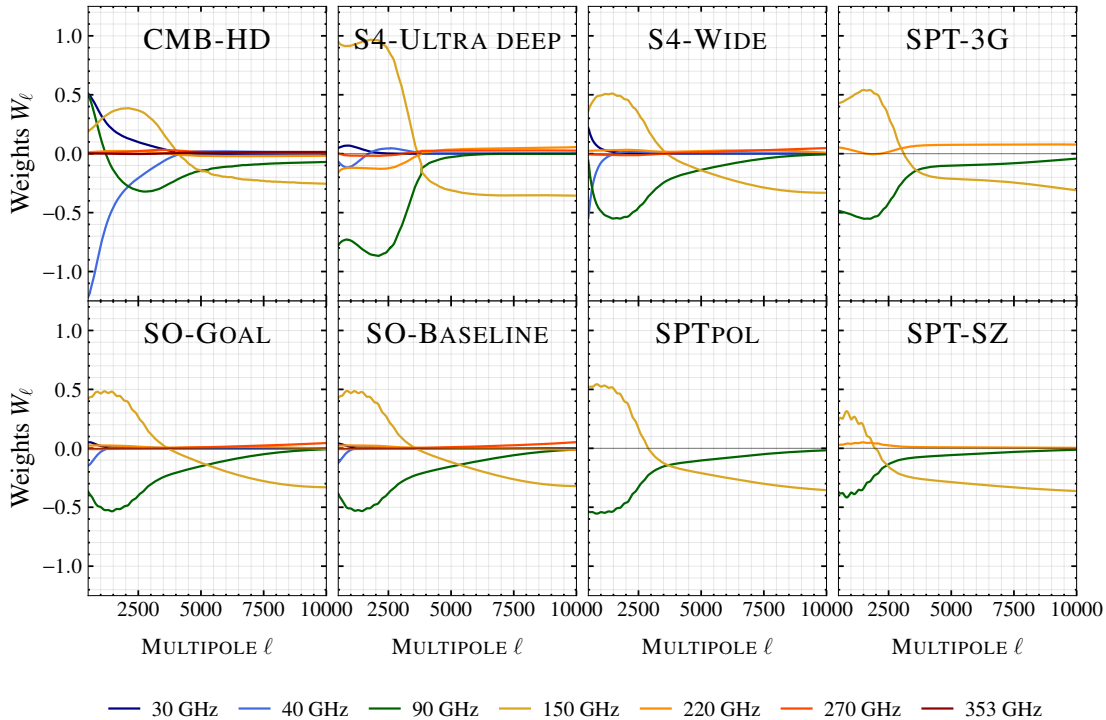


Figure 3. Multipole dependent weights for different frequency bands used to construct the minimum variance Compton- y map from different experiments considered in this work. The weights are dominated by 90 and 150 GHz channels. At large-scales, 30 and 40 GHz can add some information due to the reduced level of atmospheric noise. Bands higher than 220 GHz are primarily used to reduce the variance from CIB.

majority of the clusters at all redshifts. Finally, the covariance matrix $\hat{\mathbf{C}}$ is computed using $N = 2500$ simulations as

$$\hat{\mathbf{C}} = \frac{1}{N-1} \sum_{n=1}^N (\hat{\mathbf{y}}_i - \langle \hat{\mathbf{y}} \rangle) (\hat{\mathbf{y}}_i - \langle \hat{\mathbf{y}} \rangle)^T. \quad (9)$$

We decompose $\hat{\mathbf{C}}$ into two components

$$\hat{\mathbf{C}} = \hat{\mathbf{C}}_{\text{other}} + \hat{\mathbf{C}}_{\text{tSZ}}. \quad (10)$$

The first term $\hat{\mathbf{C}}_{\text{other}}$ is calculated using maps from different bands that contain CMB, noise, and all astrophysical foregrounds other than the tSZ after passing them through the ILC pipeline to get the MV Compton- y map. This Compton- y only contains all sources of noise but does not include the cluster tSZ or tSZ signals from other haloes.

As mentioned in §2.3, we inject the tSZ signals using three different approaches. For the case when we ignore tSZ-noise from all haloes (no-tSZ), we set the second term $\hat{\mathbf{C}}_{\text{tSZ}} = 0$. We calculate $\hat{\mathbf{C}}_{\text{tSZ}} \equiv \hat{\mathbf{C}}_{\text{tSZ}}^{\text{Gaussian}}$ using Gaussian realizations of the tSZ signals for the other two cases. For Poisson-tSZ, since the noise from tSZ will be lower (higher) in pixels where massive clusters are absent (present), we apply a scaling factor to $\hat{\mathbf{C}}_{\text{tSZ}}$

during the likelihood calculation. However, we do not find the results to be sensitive to the choice of this scaling factor. This simple scaling does not treat the effect of tSZ non-Gaussianities but we do not notice any bias in our results and hence consider them to be negligible. We provide more details about the scaling in Appendix A.

We perform 500 simulations and use the distribution of best-fits $\hat{\mathbf{y}}_{\text{fit}}$ to compute the S/N . Specifically, S/N is calculated as the inverse of the 1σ uncertainty defined using the 16th and the 84th percentiles. We do not use the standard deviation of the distributions to estimate the S/N as that will be dominated the non-Gaussian tails for the Poisson-tSZ case. See Appendix A for more details. Using this setup, we construct an experiment-dependent S/N look-up table for clusters in a (M_{500c}, z) grid and use that to estimate the limiting cluster mass that satisfies the detection threshold $S/N \geq 5$ as a function of redshift for each experiment. The (M_{500c}, z) grid we chose is: $\Delta \log(M_{500c}/M_{\odot}) \in [13, 15.4]$ with $\Delta \log(M/M_{\odot}) = 0.1$ and $z \in [0.1, 3]$ with $\Delta z = 0.1$.

4. FISHER FORMALISM

In this section, we describe the Fisher forecasting formalism to combine cluster counts with primary CMB TT/EE/TE spectra. We also check the gain by includ-

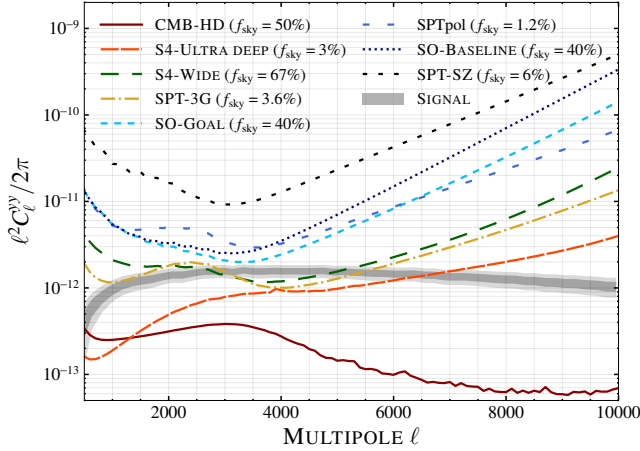


Figure 4. Noise residuals N_{ℓ}^{yy} in the Compton- y maps from different experiments considered in this work. The grey band represents the fiducial signal level from simulations with $1\sigma, 2\sigma$ errors from the SPT-SZ survey (George et al. 2015). SPT-3G and S4-Wide will map the peak of the tSZ power spectrum with $S/N \geq 1$ and the S/N for S4-Ultra deep and CMB-HD are much higher. The residual noise in the Compton- y map for CMB-HD is lower than the fiducial signal level at $\ell \geq 500$ because of the reduced level of CIB signals. The small-scale noise in other experiments contains significant contributions from both CIB and instrumental noise. The sky area scanned by each experiment is also provided in the legend.

ing information from the tSZ power spectrum although the constraining power of $N(z, M_L, q)$ is higher than the tSZ spectrum since we are localizing the signal better in numerous mass, redshift, and S/N bins. The procedure is briefly described below and we refer the reader to R21 for more details.

To obtain the binned cluster counts $N(z, M_L, q)$, we use the Monte Carlo (MC) sampling approach described in R21. We choose 40 and 25 logarithmic bins for lensing mass and tSZ S/N : $M_L \in [10^{12}, 10^{16}] M_{\odot}$ and $q \in [5, 500]$. For redshift, we use $\Delta z = 0.1$ for $0.1 \leq z < 1.5$ and group all $z \geq 1.5$ clusters in one massive redshift bin. To this end, we obtain the number of haloes $n(M_{500c}, z)$ in the range $M_{500c} \in [10^{13}, 10^{16}] M_{\odot}$ with $\Delta M_{500c} = 10^{12} M_{\odot}$ and $0.1 \leq z \leq 3$ with $\Delta z = 0.1$ using Tinker et al. (2008) HMF. We assign a tSZ flux and an associated tSZ S/N q for each halo using the distributions: $\mathcal{N}(\log Y_{\text{SZ}} | M, z, \sigma_{\log Y_{\text{SZ}}})$ and $\mathcal{N}(q | Y_{\text{SZ}} / \sigma_{Y_{\text{SZ}}}, 1)$. For tSZ S/N , we use the S/N look-up table described in §3. Similarly, lensing mass and redshifts are assigned using the distributions: $\mathcal{N}(M_L | M, \sigma_{M_L})$ and $\mathcal{N}(z | z_{\text{true}}, \sigma_z)$ where σ_{M_L} is the CMB-cluster lensing mass error calculated using both CMB temperature and polarization measurements for each survey (Raghunathan et al. 2017, 2019); and the redshift errors are

assumed to be $\sigma_z = 0$. External lensing information, like for example from optical surveys, is ignored for simplicity. The derivatives $\partial N(z, M_L, q) / \partial \theta$ as a function of parameter θ for Fisher forecasts were obtained with the finite difference approach using the same setup above and the weighting schemes described in R21.

For primary CMB TT/EE/TE Fisher matrix, we use the lensed CMB spectra obtained using CAMB (Lewis et al. 2000) software for the fiducial *Planck* 2015 cosmology. Data from all bands in a given survey are optimally combined using the ILC approach. The assumptions about polarized foregrounds are similar to R21: 2% (3%) polarization fractions for DSFG (radio galaxies) consistent with measurements from ACT (Datta et al. 2018) and SPT (Gupta et al. 2019) and the diffuse kSZ/tSZ signals are assumed to be unpolarized. We use information up to $\ell_{\text{max}} = 3500$ for the current and $\ell_{\text{max}} = 5000$ for the future CMB surveys.

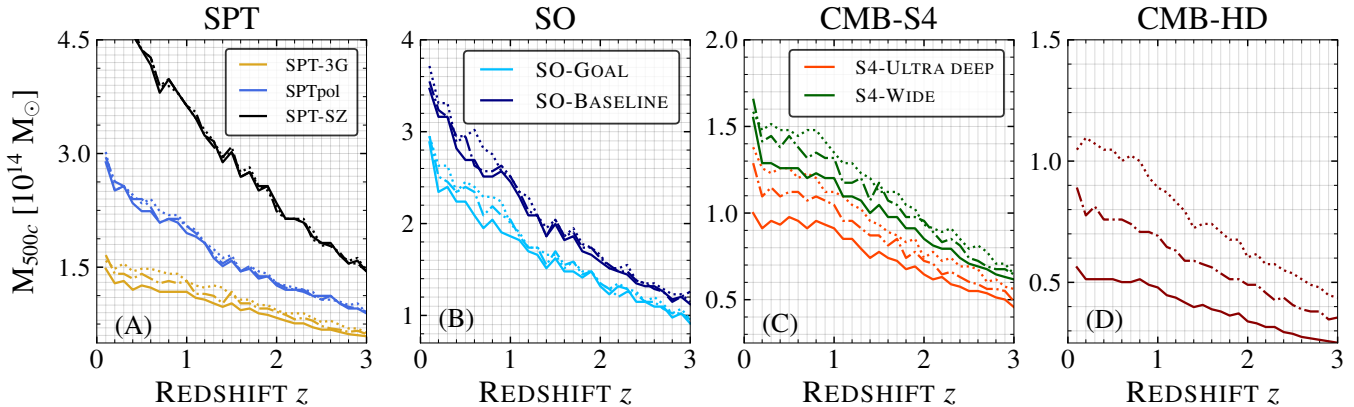
In this work, we also assess the improvement gained by including information from the tSZ power spectrum C_{ℓ}^{yy} . We obtain the C_{ℓ}^{yy} and the derivatives $\partial C_{\ell}^{yy} / \partial \theta$ using the Poisson simulations described in §2.3. Although Hurier & Lacasa (2017) argue that the correlation between $N(z, M_L, q)$ and C_{ℓ}^{yy} is minimal, we follow two approaches. In the first approach, we use the tSZ power spectrum in Fig. 2 obtained without masking any detected clusters. The second approach is highly conservative where we compute the C_{ℓ}^{yy} after masking clusters detected by the survey under consideration. Masking the detected clusters should significantly reduce the correlation between the two probes. We set $\ell_{\text{max}} = 8000$ for C_{ℓ}^{yy} .

The parameter θ constrained in this work is one of the 15 observable-mass scaling relation or cosmological parameters. The parameters governing the observable-mass scaling relation are given in Eq.(5) and Eq.(6): $\theta \in [\alpha_Y, b_{\text{HSE}}, \beta_Y, \gamma_Y, \sigma_{\log Y, 0}, \alpha_{\sigma}, \gamma_{\sigma}]$. The cosmological parameters are the 6 Λ CDM parameters along with the extension to include the sum of neutrino masses and dark energy equation of state: $\theta \in [A_s, h, \sum m_{\nu}, n_s, \Omega_c h^2, \Omega_b h^2, \tau_{\text{re}}, w_0]$. Note that we fix the normalization Y_* since it is highly degenerate with the hydrostatic mass bias parameter $1 - b_{\text{HSE}}$. Including Y_* , however, has a negligible impact on other scaling relation or cosmological parameter constraints.

5. RESULTS AND DISCUSSION

5.1. Cluster detection sensitivity

In Fig. 5 we present the minimum detectable cluster mass satisfying $S/N \geq 5$ at each redshift $z \in [0.1, 3.0]$ in bins of $\Delta z = 0.1$ for all experiments ordered from left to right based on the survey timeline. Each experiment



THERMAL SZ SIMULATIONS: — NONE --- POISSON GAUSSIAN

Figure 5. Cluster survey sensitivity expressed using the minimum detectable cluster mass at each redshift. For each experiment, the three curves correspond to different simulations of the tSZ signals: solid for no, dash-dotted for Poisson, and dotted for Gaussian-tSZ cases. For SPT-SZ, SPTpol, SO-Baseline and SO-Goal, all the three curves lie on top of each other indicating that the tSZ-noise is not important. For SPT-3G (yellow in panel A) and S4-Wide (green in panel C), although the sensitivity for the Gaussian-tSZ is worse than the other two, the difference between the three curves is small $\leq 10\%$. For CMB-HD (S4-Ultra deep) shown as darkred in panel D (orange in panel 3), the Poisson case reduces the sensitivity by 35 – 50% (10 – 15%) compared to the no-tSZ case. Switching to Gaussian-tSZ simulations can degrade the sensitivity further for these two surveys.

consists of three curves: solid for no-tSZ, dash-dotted for Poisson-tSZ, and dotted for Gaussian-tSZ cases. The difference between no (solid) and Poisson (dash-dotted) cases quantifies the impact of the tSZ-noise. The difference between the Poisson (dash-dotted) and the Gaussian (dotted) cases shows the importance of the non-Gaussian distribution of the tSZ but this is only important when the tSZ-noise is non-negligible. This can be inferred from the figure where we can note that although the S/N is worse for the Gaussian case compared to the Poisson, the level of S/N degradation depends on the experiment. As expected, the results are better in the absence of the tSZ signals (solid curves) compared to the other two cases.

For CMB-HD, assuming a Gaussian distribution of the diffuse tSZ increases the limiting mass at all redshifts by $\sim 25 - 40\%$ compared to the Poisson case. Both cases are worse than the no-diffuse tSZ case: Poisson by 40-50% and Gaussian by $\geq 80\%$. Thus, we find that the tSZ-noise can degrade the cluster S/N significantly for the CMB-HD experiment. For S4-Ultra deep, the S/N reduction for the Gaussian case compared to Poisson case is around 15%. Compared to the no-tSZ case, the Poisson case is worse by 10 – 15%, indicating that the tSZ-noise is mildly important for S4-Ultra deep. For S4-Wide and SPT-3G surveys, the difference between Gaussian and Poisson case is much smaller $\sim 5\%$ and the Poisson case is worse than the no-diffuse tSZ case

by $\lesssim 8\%$. In the case of other experiments namely SO-Goal, SO-Baseline, SPTpol or SPT-SZ, the three curves are indistinguishable and the tSZ-noise has no impact on these surveys.

The reason that the tSZ-noise has a large impact only on CMB-HD is primarily because of the reduced level of residual CIB signals in the Compton- y maps. The residual CIB is non-negligible for S4-Ultra deep and hence the impact of tSZ confusion noise is lower than CMB-HD. Both S4-Wide and SPT-3G, despite having low instrumental noise compared to current surveys, are limited by the residual CIB signals. The sensitivity of other experiments are limited by both the instrumental noise and the residual foreground signals. The importance of the noise from tSZ signals reduces when the residual noise or foreground signals increase. This is also evident from Fig. 4 where we can note that the total residual noise is roughly an order of magnitude lower than the signal (gray band) at arcminute scales for CMB-HD while that is not the case for other experiments.

5.2. Results after removing the detected clusters

Now we turn to the effect of removing the detected clusters from the maps.

5.2.1. Reduction in tSZ power after masking

Given that the detected clusters dominate the tSZ power spectrum and their number counts is highly non-Gaussian, masking the detected clusters should have an

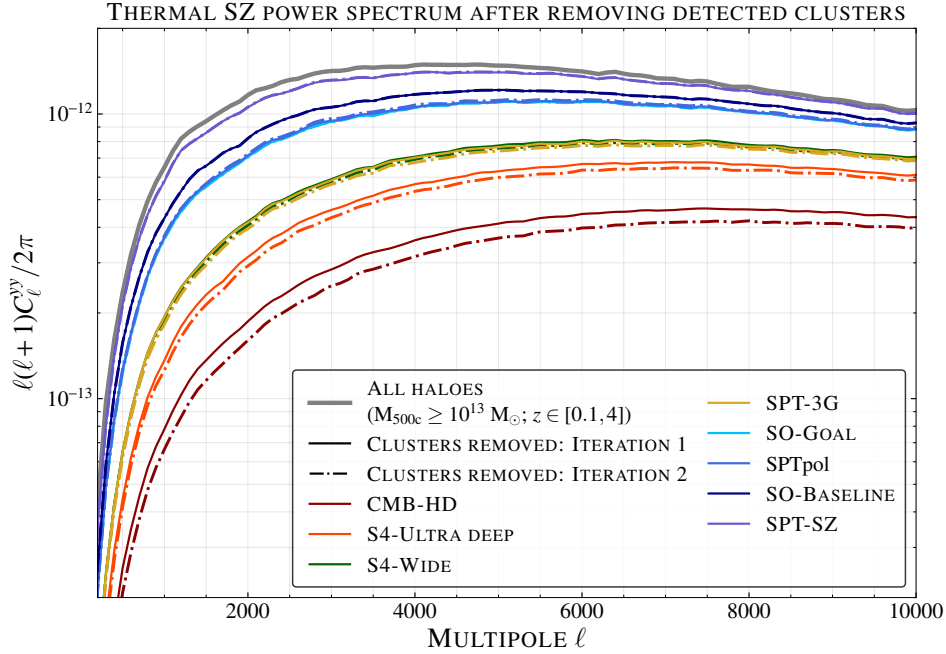


Figure 6. Impact of masking the detected clusters on the Compton- y power spectrum are shown as colored curves. For reference, the fiducial unmasked spectrum is in grey. After masking we note a suppression of the Compton- y power, measured at $\ell_{\text{norm}} = 3000$, for different experiments in the following order: CMB-HD ($\times 5$); S4-Ultra deep ($\times 3.1$); S4-Wide and SPT-3G ($\times 2.4$); SO-Goal and SPTpol ($\times 1.5$); SO-Baseline ($\times 1.35$); and SPT-SZ ($\times 1.08$). The solid and dash-dotted colored curves are for two levels of masking. The second level of masking is only important for experiments where the tSZ-noise is important namely CMB-HD and S4-Ultra deep. After second iteration, we see a further 13% (6%) suppression in the power for CMB-HD (S4-Ultra deep). All curves correspond to the median value from 500 Poisson realizations.

impact on the tSZ power spectrum. In Fig. 6, we present the resultant Compton- y power spectrum after masking clusters detected with $S/N \geq 5$ by each experiment.

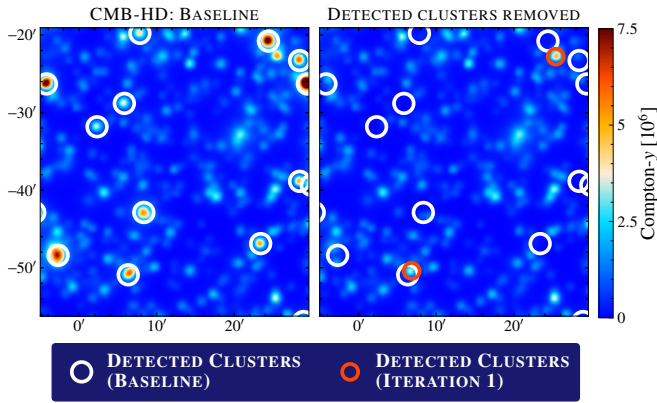


Figure 7. Zoomed-in version of the Poisson realization shown in Fig. 1. The region shown is $35' \times 35'$ wide and centered at $(\theta_x, \theta_y) = (17.3, 18.5)$. *Left panel:* Clusters detected above $S/N \geq 5$ by the CMB-HD experiment are highlighted using white circles. *Right panel:* Removing the clusters detected in the baseline case (left panel) allows us to detect new smaller (less massive or distant) clusters near the same LOS. The new detections are highlighted using red circles.

The curves represent the median value from 500 Poisson realizations. The power spectrum for the baseline case, without any masking, is shown as the thick grey curve. The masked power spectra are shown as solid curves in different shades for each experiment. The dash-dotted curves are for a second level of masking and they are discussed next. We use the value at $\ell_{\text{norm}} = 3000$ to quote the reduction in Compton- y power after cluster masking. For SPT-SZ, masking the detected clusters does not have a huge impact on the power spectrum and only reduces it by $\times 1.08$. For SO-Baseline, we find that masking the detected clusters suppresses the power by $\times 1.35$. The reduction in power is roughly similar for SPTpol ($\times 1.49$) and SO-Goal ($\times 1.51$) followed by SPT-3G and S4-Wide where the power goes down by more than a factor of two ($\times 2.4$). For S4-Ultra deep and CMB-HD, we find an even higher suppression: $\times 3.1$ and $\times 5$ respectively. Switching from median to mean value of the 500 Poisson realizations, decreases the power further by $\sim 10\%$ for all experiments. This reduction in the Compton- y power and the performance of different experiments are fully in accordance with the inference from Fig. 5.

Next, we focus on the colored dash-dotted curves in the Fig. 6 which are for the next level of cluster masking

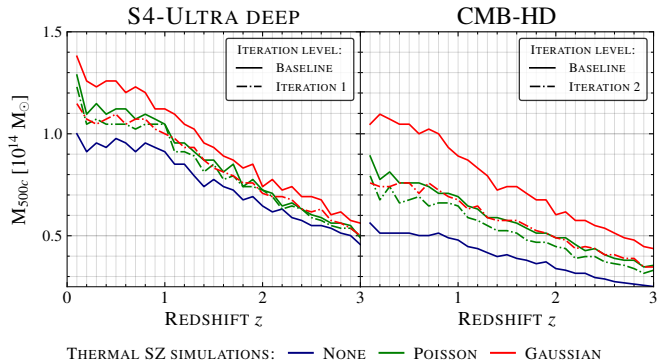


Figure 8. Change in the cluster survey sensitivity after removing the detected clusters for S4-Ultra deep (CMB-HD) in the *left* (*right*) panel. The three colors are for different simulations of the tSZ signals: blue for no, green for Poisson, and red for Gaussian. Solid and dash-dotted curves represent results from the baseline setup vs the ones after removing detected clusters. After one round of cluster removal, Poisson and Gaussian cases match for S4-Ultra deep. On the other hand, CMB-HD requires multiple iterations for the Poisson and Gaussian cases to roughly match (within $\lesssim 8\%$). Even after removing detected clusters, the Poisson-tSZ is higher than the no-tSZ case by 30% (10%) for CMB-HD (S4-Ultra deep) which represents the systematic floor set by the confusion noise from haloes below the detection limit.

(i.e.) after removing the first set of detected clusters, we re-run the cluster S/N computation to detect new clusters (see §5.2.2 below). For CMB-HD (S4-Ultra deep), a second round of masking lowers the Compton- y power further down by 13% (6%). The solid and dash-dotted lines are almost indistinguishable in Fig. 6 for other experiments, since the tSZ-noise is negligible and removing detected clusters does not help in finding new ones.

5.2.2. Survey sensitivity after removing detected clusters and the tSZ confusion noise floor

The process of removing detected clusters facilitates us to detect new clusters. This is illustrated in Fig. 7 for the CMB-HD experiment. We assume that detected clusters can be perfectly modeled and removed from the maps using a template fitting approach. This, however, is not true in reality and we will have residuals due to the mis-match between the assumed templates and the true cluster signal arising due to mergers or asymmetric cluster profiles. We ignore such complexities since we are only trying to demonstrate the proof of concept in this work. The new detections are less massive or distant clusters which were missed in the first iteration because they lie near the LOS of a more massive cluster. In the figure, the baseline case is shown in the *left* panel and the locations of clusters detected by the CMB-HD experiment are highlighted as white circles. The second

run after perfect cluster removal is shown in the *right* panel and the newly detected clusters are highlighted using red circles. The highlighted object in the bottom left is a cluster with $(M_{500c}, z) = (7 \times 10^{13} M_{\odot}, 0.7)$ and is detected in the second run after removing a $(M_{500c}, z) = (9 \times 10^{13} M_{\odot}, 0.8)$ in the same LOS. The cluster detected in the top right is superposition of two clusters: $M_{500c} \sim 6 \times 10^{13} M_{\odot}$ at $z = 1.2$ which is just below the detection threshold and another cluster $M_{500c} \sim 3 \times 10^{13} M_{\odot}$ at $z = 1.8$. Since removing the detected clusters improves the overall survey sensitivity slightly (see Fig. 8), the former is detected in the second run. This figure is the zoomed-in version ($35' \times 35'$) centered at $(\theta_x, \theta_y) = (17.3', 18.5')$ of the Poisson realization shown in Fig. 1.

Since removing the detected clusters reduces the tSZ power spectrum as shown in Fig. 6, the cluster sensitivity also improves. We quantify this improvement now and also check if multiple iterations of removing the detected clusters can help in completely eliminating the impact of noise from tSZ signals. We limit these calculations to S4-Ultra deep and CMB-HD since the tSZ-noise does not have significant impact on the other surveys. The results are presented in Fig. 8 with S4-Ultra deep in *left* and CMB-HD in *right* panels respectively. Solid lines are for the baseline case (same as Fig. 5) and dash-dotted lines are after removing the detected clusters. We compare the results from Poisson (green) and Gaussian-tSZ (red) cases for the successive iterations. The no-tSZ (blue) case is also shown in the figure for reference. The underlying power spectrum used for Gaussian realizations of the tSZ after removing detected clusters are the colored lines in Fig. 6 for the respective experiment.

For S4-Ultra deep, after the first iteration of detected-cluster removal, the Poisson and Gaussian cases roughly overlap. They are both $\sim 10\%$ above the blue (no-tSZ case) and we find no further improvement in the successive iterations. This is because the tSZ noise is now sourced from the haloes below the detection limit for S4-Ultra deep. The results are slightly different for CMB-HD on the other hand which requires two levels of cluster removal for the Poisson and Gaussian cases to match to within $\lesssim 8\%$. However, even after two rounds of masking, the green and the red curves are higher than the blue (no-tSZ) by 30%. The above results suggest that the tSZ confusion noise from haloes below the detection limit sets an ultimate floor of $\sim 30\%$ (10%) for cluster detection using CMB-HD (S4-Ultra deep). There is also a small improvement in sensitivity, ratio of green solid to dash-dotted lines, for both experiments after masking: 12% (3%) for CMB-HD (S4-Ultra deep).

Table 3. Expected number of $S/N \geq 5$ clusters from SZ surveys.

Experiment	Total clusters			z^{med}	M_{500c}^{med} [$10^{14} M_{\odot}$]
	Total	$z \geq 1.5$	$z \geq 2$		
SPT-SZ	410	7	-	0.6	3.6
SPTpol	600	24	3	0.7	2.5
SPT-3G	6935	477	80	0.7	1.3
SO-Baseline	14424	490	53	0.7	2.5
SO-Goal	26445	1256	189	0.7	2.0
S4-Wide	107747	7958	1548	0.8	1.6
S4-Ultra deep	11801	1144	231	0.8	1.0
CMB-HD	514530	79099	20682	0.9	0.6

5.2.3. Cluster counts and parameter constraints

In Table 3, we show the expected number of clusters along with the median mass M_{500c} and redshift. We also explicitly show the number of high redshift, $z \geq 1.5$ and $z \geq 2$, clusters. For S4-Wide, we ignore the regions contaminated by the galactic foregrounds and use $f_{\text{sky}} = 50\%$. The sky fractions for other surveys are given in Table 1. These calculations use the mass thresholds derived using the Poisson tSZ simulations (dash-dotted curves in Fig.5). Switching to the Gaussian-tSZ case reduces the number of clusters for CMB-HD (S4-Ultra deep) by $\times 1.8$ (1.3). On the other hand, ignoring noise due to tSZ signals from other haloes increases the total clusters by $\times 2.3$ and $\times 1.4$ for CMB-HD and S4-Ultra deep respectively. The impact due to the choice of the tSZ signals is smaller for all the other surveys which is consistent with the mass thresholds reported above. The expected number of clusters, the median mass M_{500c}^{med} , and the median redshift z^{med} obtained in this work are in reasonable agreement with other works in the literature, for example, the published SPT-SZ catalog by Bleem et al. (2015) and the forecasts presented by The Simons Observatory Collaboration et al. (2018) for the two SO configurations.

We use the cluster counts and combine them with the primary CMB TT/EE/TE spectra to obtain parameter constraints. The results with the inclusion of tSZ power spectrum is discussed next. If Fig. 9, we show the marginalized parameter constraints for $\theta \in [A_s, h, \Omega_c h^2, \sum m_\nu, w_0]$. We limit these to the current (SPT-3G) and future (SO-Baseline, S4-Wide, S4-Ultra deep and CMB-HD) surveys. We find that all the surveys can reduce the uncertainties on A_s , h , $\Omega_c h^2$ and

the hydrostatic mass bias $1 - b_{\text{HSE}}$ to sub-percent levels. In addition, SPT-3G and SO-Baseline can reduce $\sigma(w_0)$ to $\lesssim 2\%$. On the other hand, CMB-S4 and CMB-HD can obtain sub-percent level constraints on $\sigma(w_0)$. Assuming a normal hierarchy, both the surveys can also enable a $3 - 5\sigma$ detection of the sum of neutrinos masses. The constraints, $\sigma(\sum m_\nu)$ in particular, depends on the choice of prior used for $\sigma(\tau_{\text{re}})$. Swapping the baseline *Planck*-like prior $\sigma(\tau_{\text{re}}) = 0.007$ to LiteBIRD-like prior $\sigma(\tau_{\text{re}}) = 0.002$ (no prior) improves (degrades) $\sigma(\sum m_\nu)$ by $\times 1.3 - 1.5$.

When the noise from tSZ signals are fully ignored, the CMB-HD (S4-Ultra deep) constraints improve only by 10 – 15% (5 – 10%) for all parameters. Although the number of clusters go up by significantly in this case as mentioned above, their impact on parameter constraints is only marginal. This is because the constraints are driven by the different parameter degeneracy directions between clusters vs CMB and including less massive haloes by lowering the mass thresholds does not improve the constraining power significantly.

Now, we present the improvement in the constraining power with the addition of the tSZ power spectrum. We check the results with both the unmasked C_ℓ^{yy} (black curve in Fig. 2) and C_ℓ^{yy} after masking detected clusters in each survey (colored curves in Fig. 6). Note that masking the detected clusters should significantly reduce the correlation between cluster counts and C_ℓ^{yy} . As mentioned in §4, we use $\ell_{\text{max}} = 8000$ for C_ℓ^{yy} . While small-scale residual CIB signals can be potentially problematic and need to be carefully modeled, we ignore CIB modeling given that the improvement after adding C_ℓ^{yy} is not dramatic. The maximum constraining power is for $\sigma(\Omega_c h^2)$ which improves by 20 – 25% (8 – 10%) for all surveys with the unmasked (masked) C_ℓ^{yy} . For other parameters, the improvement is $\lesssim 10\%$ even in the optimistic case of using the unmasked C_ℓ^{yy} .

6. CONCLUSION

We assessed the importance of noise from tSZ signals, arising from the haloes along the LOS and the ones below the detection limit, for cluster detection from a variety of CMB surveys ranging from the past to the future namely: SPT-SZ, SPTpol, SPT-3G, SO-Baseline, SO-Goal, S4-Wide, S4-Ultra deep and CMB-HD. The framework involved three different ways of injecting the tSZ signals into the simulated maps which contain CMB, experimental noise, and other astrophysical foregrounds. The tSZ simulations includes contribution from all haloes in the mass range $M_{500c} \geq 10^{13} M_{\odot}$ at redshifts $z \in [0.1, 4.0]$ and are simulated either as Poisson or as Gaussian realizations. For Poisson realizations,

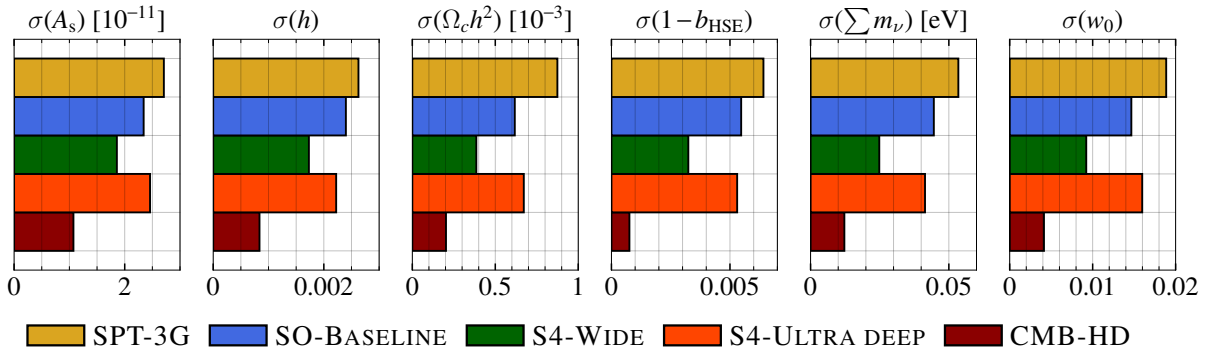


Figure 9. Marginalized parameter constraints for the current (SPT-3G) and future (SO-Baseline, S4-Wide, S4-Ultra deep and CMB-HD) surveys obtained by combining cluster abundance measurements and the lensed CMB power spectra (TT/EE/TE). A *Planck*-like prior $\sigma(\tau_{re}) = 0.007$ has been assumed in all cases. We find that the all surveys can obtain $\lesssim 1\%$ constraints on $\sigma(A_s)$, $\sigma(h)$, $\sigma(\Omega_c h^2)$ and $\sigma(1 - b_{HSE})$. Furthermore, the errors on $\sigma(w_0)$ can be reduced to $\leq 2\%$ in the next few years by SPT-3G and SO-Baseline. CMB-S4 and CMB-HD can strengthen these measurements further by reducing $\sigma(w_0)$ to sub-percent levels and by enabling a $3 - 5\sigma$ detection of the sum of neutrino masses.

we adopt [Tinker et al. \(2008\)](#) HMF to get the halo number counts and model the cluster tSZ signal using the generalized NFW profile. The power spectrum of the Poisson realizations was used to generate Gaussian realizations. We compared these results with the ones where the tSZ signals (no-tSZ) are fully ignored. The difference between Poisson and the no-tSZ cases was used to quantify the importance of the noise from tSZ signals.

Our results indicated that the tSZ-noise has a significant impact (35 – 50%) only on the CMB-HD experiment and mildly (10 – 15%) affects CMB-S4’s delensing (S4-Ultra deep) survey. For all the other experiments, the tSZ signals either have no impact (SPT-SZ, SPTpol, SO-Baseline and SO-Goal) or lead to minor (SPT-3G and S4-Wide) differences in the results compared to the no-tSZ case. This is because the Compton- y maps of these experiments are dominated by residual experimental noise or other astrophysical foregrounds which are much higher than fiducial tSZ signal level.

In all cases, we found that the Poisson-tSZ case returns a higher S/N than the Gaussian-tSZ case for a given cluster. This, however, is only important when the tSZ-noise has a large impact in the survey sensitivity. In other words, performing a Gaussian realization of the tSZ signals: (a) does not have any impact on SPT-SZ, SPTpol, SO-Baseline and SO-Goal; (b) can slightly (5 – 10%) worsen the results for SPT-3G and S4-Wide; and (c) can significantly affect S4-Ultra deep (15 – 20%) and CMB-HD ($\geq 80\%$).

We also quantified the impact of masking the detected clusters on the tSZ power spectrum for all the surveys. The reduction in the power is quoted at $\ell_{norm} = 3000$. Compared to the original (unmasked) case, the power spectrum goes down by: $\times 5$ for CMB-HD; $\times 3.1$ of S4-

Ultra deep; $\times 2.4$ for S4-Wide and SPT-3G; $\times 1.5$ for SO-Goal and SPTpol; $\times 1.35$ for SO-Baseline; and $\times 1.08$ for SPT-SZ. This reduction can have important implications for detecting the kSZ power spectrum in the small-scale CMB TT power spectrum for current and future CMB surveys since the amplitude of the kSZ is degenerate with that of the tSZ (see for example, [Dunkley et al. 2013](#); [George et al. 2015](#); [Reichardt et al. 2021](#)).

We also showed that a perfect removal of the detected clusters can help us detect less massive and distant clusters that lie near the LOS of the removed clusters. Removing the detected clusters also improved the cluster survey sensitivity slightly by $\sim 12\%$ (3%) for CMB-HD (S4-Ultra deep). The improvement saturates after two (one) round of cluster removal and the tSZ confusion noise, sourced by haloes below the detection limit, sets a floor of 30% (10%) for cluster detection using CMB-HD (S4-Ultra deep) compared to the case when tSZ signals are fully ignored.

We forecasted the expected number of clusters from all the surveys finding significant improvement in the sample size compared to the currently available SZ catalogs. Finally, we combined the cluster abundance measurements with primary CMB TT/EE/TE and tSZ power spectra to obtain constraints on cluster observable-mass scaling relation and cosmological parameters for current and future surveys. In the next few years, SPT-3G and SO will be able to constrain the error on the dark energy equation of state parameter $\sigma(w_0)$ to an accuracy level of $\leq 2\%$. The CMB-S4 experiment, in the next decade, can improve the accuracy on $\sigma(w_0)$ to sub-percent levels and also enable a 3σ detection of the sum of neutrino masses $\sum m_\nu$. The futuristic CMB-HD survey will add further constraining power and is also capable of detect-

ing $\sum m_\nu$ at $\geq 5\sigma$. The simulation products and results are publicly available and can be downloaded from this [link](#).

ACKNOWLEDGMENTS

I am indebted to Gil Holder and Nathan Whitehorn for their feedback and suggestions throughout the course of this work. I also thank Tom Crawford, Daisuke Nagai, Yuuki Omori and Christian Reichardt for useful discussions and their feedback on the manuscript. Finally, I thank the anonymous referee for useful suggestions that helped in shaping this manuscript better. I acknowl-

edge the support by the Illinois Survey Science Fellowship from the Center for AstroPhysical Surveys at the National Center for Supercomputing Applications.

This work made use of the Illinois Campus Cluster, a computing resource that is operated by the Illinois Campus Cluster Program (ICCP) in conjunction with the National Center for Supercomputing Applications (NCSA) and which is supported by funds from the University of Illinois at Urbana-Champaign. This work also used the computational and storage services associated with the Hoffman2 Shared Cluster provided by UCLA Institute for Digital Research and Education's Research Technology Group.

APPENDIX

A. SIGNAL-TO-NOISE CALCULATION

We discuss the S/N calculation for the three cases of tSZ simulations here. Fig. A1 shows the distribution of the best-fit values from 500 simulations for the three kinds of tSZ simulations: no-tSZ in blue (panel A), Poisson-tSZ in green (panels B through E), and Gaussian-tSZ in red (panel F). We report the best-fit values in terms of M_{500c} here. The 16th and the 84th percentiles values of these distributions are used to estimate the S/N in each case. We choose this rather than the standard deviations to account for the non-Gaussian tails, which is evident from the figure for the Poisson cases in green. The widths calculated this way are σ_{actual} and marked in all panels. The standard deviations of the distributions, assuming Gaussianity, are σ_{Gau} . As expected, $\sigma_{\text{Gau}} = \sigma_{\text{actual}}$ for blue (no-tSZ) and red (Gaussian-tSZ) but $\sigma_{\text{Gau}} > \sigma_{\text{actual}}$ for green (Poisson-tSZ). To guide the eye, we also show a simple Gaussian fit with width $\sigma = \sigma_{\text{actual}}$ using a black dashed line. For this illustration, we choose a cluster with $(M_{500c}, z) = (0.794 \times 10^{14} M_\odot, 0.7)$ as seen by the CMB-HD experiment. Note from the figure that the $S/N = 1/\sigma_{\text{actual}} = 3.6$ for this cluster is below the detection limit for the Gaussian-tSZ case but improves to $S/N = 5.9$ when we switch to the Poisson-tSZ simulations.

The values of α marked as titles are the factors applied to scale the tSZ covariance matrix $\hat{\mathbf{C}}_{\text{tSZ}}^{\text{Gaussian}}$ used in the likelihood calculation (see Eq: 10) and estimated using Gaussian simulations of the tSZ signal. For the no-tSZ (panel A in blue) and Gaussian-tSZ (panel F in red) cases, we set $\alpha = 0$ and $\alpha = 1$. For the Poisson case, since the map variance

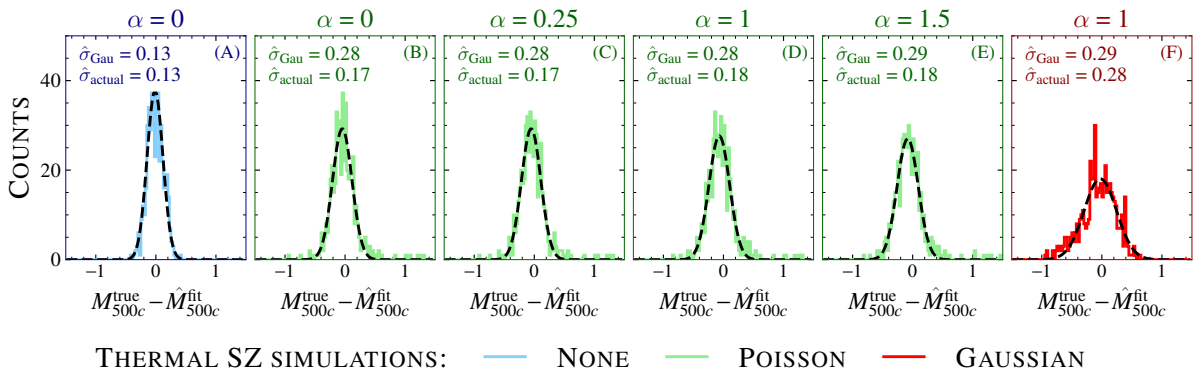


Figure A1. Distribution of the difference between the true and best-fit mass values from 500 simulations for the three cases of tSZ simulations: blue (no), green (Poisson), and red (Gaussian). For blue and red, the distributions are well fit by a Gaussian with $\sigma = \sigma_{\text{Gau}}$ but the non-Gaussian tails are clear for green (Poisson case). The actual σ_{actual} calculated using the 16th and the 84th percentiles of the distributions is also shown for all cases: $\sigma_{\text{actual}} = \sigma_{\text{Gau}}$ for blue and red but $\sigma_{\text{actual}} < \sigma_{\text{Gau}}$ for green. For the Poisson case, we show the distributions for four different scalings of $\hat{\mathbf{C}}_{\text{tSZ}}^{\text{Gaussian}}$: $\alpha \in [0, 0.25, 1, 1.5]$. While the choice of α modifies the non-Gaussian tails for green panels, it does not affect σ_{actual} . We pick a cluster with $(M_{500c}, z) = (0.794 \times 10^{14} M_\odot, 0.7)$ for this demonstration and use the best-fit distributions from the CMB-HD experiment.

is dominated by the few pixels with clusters, we test the results by arbitrarily scaling the $\hat{C}_{tSZ}^{\text{Gaussian}}$ using different values of $\alpha \in [0, 0.25, 1, 1.5]$. While the choice of α modifies the non-Gaussian tails, it does not affect σ_{actual} as can be inferred from green colored panels (B) through (E). This simple scaling does not handle the effect of non-Gaussianities. However, given that we do not observe any bias, we assume the impact of the non-Gaussianities to be negligible and ignore them.

REFERENCES

- Allen, S. W., Evrard, A. E., & Mantz, A. B. 2011, *ARA&A*, 49, 409, doi: [10.1146/annurev-astro-081710-102514](https://doi.org/10.1146/annurev-astro-081710-102514)
- Arnaud, M., Pratt, G. W., Piffaretti, R., et al. 2010, *A&A*, 517, A92+, doi: [10.1051/0004-6361/200913416](https://doi.org/10.1051/0004-6361/200913416)
- Aylor, K., Joy, M., Knox, L., et al. 2019, *ApJ*, 874, 4, doi: [10.3847/1538-4357/ab0898](https://doi.org/10.3847/1538-4357/ab0898)
- Battaglia, N., Bond, J. R., Pfrommer, C., & Sievers, J. L. 2012, *ApJ*, 758, 75, doi: [10.1088/0004-637X/758/2/75](https://doi.org/10.1088/0004-637X/758/2/75)
- Bender, A. N., Ade, P. A. R., Ahmed, Z., et al. 2018, in *Society of Photo-Optical Instrumentation Engineers (SPIE) Conference Series*, Vol. 10708, Millimeter, Submillimeter, and Far-Infrared Detectors and Instrumentation for Astronomy IX, 1070803, doi: [10.1117/12.2312426](https://doi.org/10.1117/12.2312426)
- Benson, B. A., Ade, P. A. R., Ahmed, Z., et al. 2014, in *Society of Photo-Optical Instrumentation Engineers (SPIE) Conference Series*, Vol. 9153, Society of Photo-Optical Instrumentation Engineers (SPIE) Conference Series, 1, doi: [10.1117/12.2057305](https://doi.org/10.1117/12.2057305)
- Bhattacharya, S., Nagai, D., Shaw, L., Crawford, T., & Holder, G. P. 2012, *ApJ*, 760, 5, doi: [10.1088/0004-637X/760/1/5](https://doi.org/10.1088/0004-637X/760/1/5)
- Bleem, L. E., Stalder, B., de Haan, T., et al. 2015, *The Astrophysical Journal Supplement Series*, 216, 27, doi: [10.1088/0067-0049/216/2/27](https://doi.org/10.1088/0067-0049/216/2/27)
- Bleem, L. E., Bocquet, S., Stalder, B., et al. 2020, *ApJS*, 247, 25, doi: [10.3847/1538-4365/ab6993](https://doi.org/10.3847/1538-4365/ab6993)
- Bleem, L. E., Crawford, T. M., Ansarinejad, B., et al. 2021, arXiv e-prints. <https://arxiv.org/abs/2102.05033>
- Bocquet, S., Dietrich, J. P., Schrabback, T., et al. 2019, *ApJ*, 878, 55, doi: [10.3847/1538-4357/ab1f10](https://doi.org/10.3847/1538-4357/ab1f10)
- Bolliet, B., Comis, B., Komatsu, E., & Macías-Pérez, J. F. 2018, *MNRAS*, 477, 4957, doi: [10.1093/mnras/sty823](https://doi.org/10.1093/mnras/sty823)
- Cardoso, J.-F., Le Jeune, M., Delabrouille, J., Betoule, M., & Patanchon, G. 2008, *IEEE Journal of Selected Topics in Signal Processing*, 2, 735, doi: [10.1109/JSTSP.2008.2005346](https://doi.org/10.1109/JSTSP.2008.2005346)
- Chluba, J., Nagai, D., Sazonov, S., & Nelson, K. 2012, *MNRAS*, 426, 510, doi: [10.1111/j.1365-2966.2012.21741.x](https://doi.org/10.1111/j.1365-2966.2012.21741.x)
- CMB-S4 Collaboration. 2019, arXiv e-prints. <https://arxiv.org/abs/1907.04473>
- Costanzi, M., Saro, A., Bocquet, S., et al. 2021, *PhRvD*, 103, 043522, doi: [10.1103/PhysRevD.103.043522](https://doi.org/10.1103/PhysRevD.103.043522)
- Crawford, T. M., Schaffer, K. K., Bhattacharya, S., et al. 2014, *ApJ*, 784, 143, doi: [10.1088/0004-637X/784/2/143](https://doi.org/10.1088/0004-637X/784/2/143)
- Datta, R., Aiola, S., Choi, S. K., et al. 2018, *MNRAS*, 2799, doi: [10.1093/mnras/sty2934](https://doi.org/10.1093/mnras/sty2934)
- Douspis, M., Salvati, L., Gorce, A., & Aghanim, N. 2021, arXiv e-prints, arXiv:2111.01639. <https://arxiv.org/abs/2111.01639>
- Dunkley, J., Calabrese, E., Sievers, J., et al. 2013, *JCAP*, 2013, 025, doi: [10.1088/1475-7516/2013/07/025](https://doi.org/10.1088/1475-7516/2013/07/025)
- Everett, W. B., Zhang, L., Crawford, T. M., et al. 2020, *ApJ*, 900, 55, doi: [10.3847/1538-4357/ab9df7](https://doi.org/10.3847/1538-4357/ab9df7)
- George, E. M., Reichardt, C. L., Aird, K. A., et al. 2015, *ApJ*, 799, 177, doi: [10.1088/0004-637X/799/2/177](https://doi.org/10.1088/0004-637X/799/2/177)
- Gupta, N., Porciani, C., & Basu, K. 2020, arXiv e-prints. <https://arxiv.org/abs/2003.09069>
- Gupta, N., Reichardt, C. L., Ade, P. A. R., et al. 2019, arXiv e-prints, arXiv:1907.02156. <https://arxiv.org/abs/1907.02156>
- Henderson, S. W., Allison, R., Austermann, J., et al. 2016, *Journal of Low Temperature Physics*, 184, 772, doi: [10.1007/s10909-016-1575-z](https://doi.org/10.1007/s10909-016-1575-z)
- Henning, J. W., Sayre, J. T., Reichardt, C. L., et al. 2018, *ApJ*, 852, 97, doi: [10.3847/1538-4357/aa9ff4](https://doi.org/10.3847/1538-4357/aa9ff4)
- Hill, J. C., Baxter, E. J., Lidz, A., Greco, J. P., & Jain, B. 2018, *PhRvD*, 97, 083501, doi: [10.1103/PhysRevD.97.083501](https://doi.org/10.1103/PhysRevD.97.083501)
- Hill, J. C., & Pajer, E. 2013, *PhRvD*, 88, 063526, doi: [10.1103/PhysRevD.88.063526](https://doi.org/10.1103/PhysRevD.88.063526)
- Hill, J. C., & Sherwin, B. D. 2013, *PhRvD*, 87, 023527, doi: [10.1103/PhysRevD.87.023527](https://doi.org/10.1103/PhysRevD.87.023527)
- Hilton, M., Sifón, C., Naess, S., et al. 2020, arXiv e-prints. <https://arxiv.org/abs/2009.11043>
- Holder, G., Haiman, Z., & Mohr, J. J. 2001, *ApJL*, 560, L111, doi: [10.1086/324309](https://doi.org/10.1086/324309)
- Holder, G. P., McCarthy, I. G., & Babul, A. 2007, *MNRAS*, 382, 1697, doi: [10.1111/j.1365-2966.2007.12430.x](https://doi.org/10.1111/j.1365-2966.2007.12430.x)
- Horowitz, B., & Seljak, U. 2017, *MNRAS*, 469, 394, doi: [10.1093/mnras/stx766](https://doi.org/10.1093/mnras/stx766)
- Huang, N., Bleem, L. E., Stalder, B., et al. 2020, *AJ*, 159, 110, doi: [10.3847/1538-3881/ab6a96](https://doi.org/10.3847/1538-3881/ab6a96)

- Hurier, G., & Lacasa, F. 2017, *A&A*, 604, A71, doi: [10.1051/0004-6361/201630041](https://doi.org/10.1051/0004-6361/201630041)
- Itoh, N., Kohyama, Y., & Nozawa, S. 1998, *ApJ*, 502, 7, doi: [10.1086/305876](https://doi.org/10.1086/305876)
- Komatsu, E., & Kitayama, T. 1999, *ApJL*, 526, L1, doi: [10.1086/312364](https://doi.org/10.1086/312364)
- Komatsu, E., & Seljak, U. 2002, *MNRAS*, 336, 1256, doi: [10.1046/j.1365-8711.2002.05889.x](https://doi.org/10.1046/j.1365-8711.2002.05889.x)
- Laureijs, R., Amiaux, J., Arduini, S., et al. 2011, arXiv e-prints. <https://arxiv.org/abs/1110.3193>
- Lewis, A., Challinor, A., & Lasenby, A. 2000, *ApJ*, 538, 473, doi: [10.1086/309179](https://doi.org/10.1086/309179)
- Lima, M., & Hu, W. 2004, *PhRvD*, 70, 043504, doi: [10.1103/PhysRevD.70.043504](https://doi.org/10.1103/PhysRevD.70.043504)
- Louis, T., & Alonso, D. 2017, *PhRvD*, 95, 043517, doi: [10.1103/PhysRevD.95.043517](https://doi.org/10.1103/PhysRevD.95.043517)
- Louis, T., Grace, E., Hasselfield, M., et al. 2017, *JCAP*, 2017, 031, doi: [10.1088/1475-7516/2017/06/031](https://doi.org/10.1088/1475-7516/2017/06/031)
- LSST Science Collaboration, Abell, P. A., Allison, J., et al. 2009, ArXiv e-prints. <https://arxiv.org/abs/0912.0201>
- Madhavacheril, M. S., Battaglia, N., & Miyatake, H. 2017, *PhRvD*, 96, 103525, doi: [10.1103/PhysRevD.96.103525](https://doi.org/10.1103/PhysRevD.96.103525)
- Madhavacheril, M. S., Hill, J. C., Naess, S., et al. 2020, *PhRvD*, 102, 023534, doi: [10.1103/PhysRevD.102.023534](https://doi.org/10.1103/PhysRevD.102.023534)
- Mak, D. S. Y., & Pierpaoli, E. 2013, *PhRvD*, 87, 103518, doi: [10.1103/PhysRevD.87.103518](https://doi.org/10.1103/PhysRevD.87.103518)
- Makiya, R., Hikage, C., & Komatsu, E. 2020, *PASJ*, 72, 26, doi: [10.1093/pasj/psz147](https://doi.org/10.1093/pasj/psz147)
- Mantz, A. B., Morris, R. G., Allen, S. W., et al. 2021, *MNRAS*, doi: [10.1093/mnras/stab3390](https://doi.org/10.1093/mnras/stab3390)
- McCarthy, I. G., Bird, S., Schaye, J., et al. 2018, *MNRAS*, 476, 2999, doi: [10.1093/mnras/sty377](https://doi.org/10.1093/mnras/sty377)
- McCarthy, I. G., Le Brun, A. M. C., Schaye, J., & Holder, G. P. 2014, *MNRAS*, 440, 3645, doi: [10.1093/mnras/stu543](https://doi.org/10.1093/mnras/stu543)
- McCarthy, I. G., Schaye, J., Bird, S., & Le Brun, A. M. C. 2017, *MNRAS*, 465, 2936, doi: [10.1093/mnras/stw2792](https://doi.org/10.1093/mnras/stw2792)
- Merloni, A., Predehl, P., Becker, W., et al. 2012, ArXiv e-prints. <https://arxiv.org/abs/1209.3114>
- Nagai, D., Kravtsov, A. V., & Vikhlinin, A. 2007, *ApJ*, 668, 1, doi: [10.1086/521328](https://doi.org/10.1086/521328)
- Navarro, J. F., Frenk, C. S., & White, S. D. M. 1996, *ApJ*, 462, 563, doi: [10.1086/177173](https://doi.org/10.1086/177173)
- Planck Collaboration, Ade, P. A. R., Aghanim, N., et al. 2014, *A&A*, 571, A12, doi: [10.1051/0004-6361/201321580](https://doi.org/10.1051/0004-6361/201321580)
- . 2016a, *A&A*, 594, A27, doi: [10.1051/0004-6361/201525823](https://doi.org/10.1051/0004-6361/201525823)
- . 2016b, *A&A*, 594, A13, doi: [10.1051/0004-6361/201525830](https://doi.org/10.1051/0004-6361/201525830)
- . 2016c, *A&A*, 594, A24, doi: [10.1051/0004-6361/201525833](https://doi.org/10.1051/0004-6361/201525833)
- Planck Collaboration, Aghanim, N., Akrami, Y., et al. 2020, *A&A*, 641, A6, doi: [10.1051/0004-6361/201833910](https://doi.org/10.1051/0004-6361/201833910)
- Raghunathan, S., Holder, G. P., Bartlett, J. G., et al. 2019, *JCAP*, 2019, 037, doi: [10.1088/1475-7516/2019/11/037](https://doi.org/10.1088/1475-7516/2019/11/037)
- Raghunathan, S., Patil, S., Baxter, E. J., et al. 2017, *JCAP*, 8, 030, doi: [10.1088/1475-7516/2017/08/030](https://doi.org/10.1088/1475-7516/2017/08/030)
- Raghunathan, S., Whitehorn, N., Alvarez, M. A., et al. 2021, arXiv e-prints, arXiv:2107.10250. <https://arxiv.org/abs/2107.10250>
- Reichardt, C. L., Shaw, L., Zahn, O., et al. 2012, *ApJ*, 755, 70, doi: [10.1088/0004-637X/755/1/70](https://doi.org/10.1088/0004-637X/755/1/70)
- Reichardt, C. L., Patil, S., Ade, P. A. R., et al. 2021, *ApJ*, 908, 199, doi: [10.3847/1538-4357/abd407](https://doi.org/10.3847/1538-4357/abd407)
- Remazeilles, M., Delabrouille, J., & Cardoso, J.-F. 2011, *MNRAS*, 410, 2481, doi: [10.1111/j.1365-2966.2010.17624.x](https://doi.org/10.1111/j.1365-2966.2010.17624.x)
- Salvati, L., Saro, A., Bocquet, S., et al. 2021, arXiv e-prints, arXiv:2112.03606. <https://arxiv.org/abs/2112.03606>
- Sartoris, B., Borgani, S., Rosati, P., & Weller, J. 2012, *MNRAS*, 423, 2503, doi: [10.1111/j.1365-2966.2012.21064.x](https://doi.org/10.1111/j.1365-2966.2012.21064.x)
- Sehgal, N., Aiola, S., Akrami, Y., et al. 2019, in *BAAS*, Vol. 51, 6. <https://arxiv.org/abs/1906.10134>
- Shaw, L. D., Nagai, D., Bhattacharya, S., & Lau, E. T. 2010, *ApJ*, 725, 1452, doi: [10.1088/0004-637X/725/2/1452](https://doi.org/10.1088/0004-637X/725/2/1452)
- Shaw, L. D., Zahn, O., Holder, G. P., & Doré, O. 2009, *ApJ*, 702, 368, doi: [10.1088/0004-637X/702/1/368](https://doi.org/10.1088/0004-637X/702/1/368)
- Sunyaev, R. A., & Zel'dovich, Y. B. 1970, *Comments on Astrophysics and Space Physics*, 2, 66
- Tanimura, H., Douspis, M., Aghanim, N., & Salvati, L. 2022, *MNRAS*, 509, 300, doi: [10.1093/mnras/stab2956](https://doi.org/10.1093/mnras/stab2956)
- The Simons Observatory Collaboration, Ade, P., Aguirre, J., et al. 2018, ArXiv e-prints. <https://arxiv.org/abs/1808.07445>
- Tinker, J., Kravtsov, A. V., Klypin, A., et al. 2008, *ApJ*, 688, 709, doi: [10.1086/591439](https://doi.org/10.1086/591439)
- To, C., Krause, E., Rozo, E., et al. 2021, *PhRvL*, 126, 141301, doi: [10.1103/PhysRevLett.126.141301](https://doi.org/10.1103/PhysRevLett.126.141301)
- Zhao, H. 1996, *MNRAS*, 278, 488, doi: [10.1093/mnras/278.2.488](https://doi.org/10.1093/mnras/278.2.488)
- Zubeldia, Í., & Challinor, A. 2019, arXiv e-prints, arXiv:1904.07887. <https://arxiv.org/abs/1904.07887>